

# Study on the flow characteristics in the non-detonation reaction zones of wedge-induced oblique detonation transitions

Yue Huang <sup>a,\*</sup>, Zhenye Luan <sup>a</sup>, Zhimin Li <sup>a</sup>, Hua Ji <sup>b</sup>, Yancheng You <sup>a</sup>

<sup>a</sup> School of Aerospace Engineering, Xiamen University, Xiamen, 361005, China

<sup>b</sup> CFDART Inc., Waterloo, ON, N2T 2J6, Canada



## ARTICLE INFO

### Article history:

Received 7 May 2021

Received in revised form 27 September 2021

Accepted 8 December 2021

Available online 14 December 2021

Communicated by Yu Lv

### Keywords:

Oblique detonation wave

Bertrand-intrinsic coordinate system

Numerical simulation

Initiation structures

## ABSTRACT

Wedge-induced oblique detonation transitions are simulated numerically to investigate the non-detonation reaction zone structures that include induction and deflagration regions. Compressible reactive Euler equations are solved using a seventh-order Weighted Essentially Non-Oscillatory (WENO) scheme on an adaptive mesh. Quasi-one-dimensional primitive variables along the streamline of oblique detonation are used to study the flow characteristics inside the non-detonation reaction zones of different types of initiation structures. For a smooth transition, the fluid along the streamline of the entire non-detonation zone is in an expansion state. The gradual increase in the oblique shock angle during the pressure wave's upward movement is the primary reason for the reaction length reduction along the  $y$ -direction. For a weak abrupt-type transition, the fluid near the wedge surface is in a state of expansion. Along the  $y$ -direction, the gradual increase in the oblique shock angle and the compressibility of the fluid ahead of the main reaction zone are the two main reasons for the reduction in reaction length. For a strong-abrupt transition, the fluid near the wedge surface is still in a state of expansion. Along the  $y$ -direction, the sharp increase in the degree of compressibility ahead of the main reaction zone is the main reason for the reduction in reaction length. Comparing the reaction length of the theoretical analysis with the simulation results, it is found that the hypothesis of constant pressure combustion (CPC) along the inclined wedge surface is more appropriate than the hypothesis of constant volume combustion (CVC).

© 2021 Elsevier Masson SAS. All rights reserved.

## 1. Introduction

The stabilized oblique detonation wave (ODW) has become once more the superior combustion mode for scramjets in hypersonic flight, spurring research in oblique detonation wave engines (ODWEs). This is due to ODWE's potential advantages of greater efficiency and shorter combustor length in comparison to the traditional scramjet [1–7]. An oblique detonation wave is usually generated by a stream of supersonic uniform reactive flow passing through a wedge, which is relevant to practical configurations for hypersonic propulsion operation [5]. The initiation and stabilization of an ODW at the desired location over the entire wide flight Mach are key challenges to attaining the ODWEs performance advantages [6,7].

A wealth of analytic [1–3,8–13], experimental [4,14–17], and numerical studies [7,11,18–34] on the fundamental issues concerning an ODW induced by a wedge exists. The early theoretical solutions of oblique detonations under the different shock angles

and the ODW structures as the basic foundation were obtained by the pioneering works of Gross [8], Pratt et al. [1], Powers et al. [2,3,9], and Emanuel et al. [10] using reactive Rankine-Hugoniot analysis, in which the ODW is approximated as an oblique shock wave (OSW) coupled with an instantaneous heat release from the reaction zone. The method of characteristics with a one-step Arrhenius chemistry model was developed by Verreault et al. [11] to simulate ODW initiation from a wedge. This resulted in the determination of the wave-angle evolution. A simplified characteristics formulation of linearized Euler equations and linearized Rankine-Hugoniot jump conditions across the leading oblique shock were employed more recently by Martínez-Ruiz et al. [12,13] to analyze the OSW-ODW transition in wedge-induced oblique detonations. The characteristics of wedge-induced OSW-ODW transitions are mainly affected by reaction kinetics. A one-step Arrhenius chemistry model with sufficiently large activation energies can lead to a transition occurring at a triple point for a wide range of combinations of incoming Mach number and wedge angle. The ODW structures and different types of OSW-ODW transition were experimentally found in many references [4,14–17]. Nevertheless, the detailed flow structure of oblique detonation under different OSW-ODW transition types is difficult to describe by experimental

\* Corresponding author.

E-mail address: huangyue@xmu.edu.cn (Y. Huang).

measurement. Therefore, high-precision numerical simulation has become the main research method for oblique detonation under high Mach number conditions.

The basic formation structures of an ODW attached to a wedge were first addressed in the pioneering simulation work of Li et al. [18]; the OSW-ODW transition occurs abruptly at a triple point, which is usually referred to as the abrupt transition mode. The basic stabilization and transition structure of an ODW is qualitatively consistent with the experiments in hydrogen detonation by Viguer et al. [14,15] and Morris et al. [4]. The smooth transition mode of the OSW-ODW was first shown in the numerical simulations of Vlasenko et al. [19] and was confirmed in the numerical study by Da Silva et al. [20]. Two distinct OSW-ODW transition modes have been verified numerically for a wide range of chemical kinetics, free-stream Mach numbers, and wedge angles. Several simulations of the OSW-ODW transition have shown that increasing the free-stream Mach number for a given wedge angle favors the appearance of smooth transitions [21–23]. On the other hand, increasing the wedge angle for a given free-stream Mach number favors the appearance of abrupt transitions [24]. Approximate quantitative criteria for predicting the shift from the smooth to the abrupt transition have been proposed—criticality is associated with either a specific value of the difference between the inclination angles of the oblique shock wave and the oblique detonation [25] or a specific value for the ratio of the corresponding downstream pressures [26]. A smooth transition usually appears with a high free-stream Mach number and low activation energy without cellular structures near the initiation region. The dynamics of a transition between two smooth ODW initiation structures with a curved shock induced by a semi-infinite wedge in the high-Mach-number regime were investigated by numerical simulation by Zhang et al. [27]. The stability of an ODW with different transition patterns (i.e., smooth transition and abrupt transition) were numerically studied, systematically, by Miao et al. [28], with ODWs located in the shift area between smooth and abrupt transitions proving stable and resistant. Therefore, the types and characteristics of wedge-induced OSW-ODW transitions are mainly affected by the incoming-flight Mach number, wedge angle, and chemical kinetics. Since two-dimensional numerical simulations are computationally demanding, numerical studies tend to focus on a limited number of cases (e.g., by fixing the wedge angle or the incoming stream's properties), so that only limited portions of the accessible parametric space are explored. As a result, despite significant work, a complete parametric specification of the conditions under which different types of OSW-ODW transitions may occur is still lacking.

The structure of ODWs has often been investigated, but the emphasis has always been placed on the conditions under which different transition patterns occur. However, the structures of non-detonation reaction zones and the differences between ODWs with different transition patterns have been rarely researched. The induction zone length and transition wedge angle between the kinetics-controlled and wave-controlled initiation modes of the wedge-induced ODW were simulated using a finite-length wedge by Teng et al. [21] and the hypothesis of CVC along the inclined wedge surface was used to calculate the initiation length of the ODW. The effects of activation energy on the evolution of ODW structure during different OSW-ODW transitions were simulated by Zhang et al. [29] using inviscid Euler equations with a one-step irreversible Arrhenius chemistry model. They found two types of structures: one, a saw-tooth reactive front, and another, a keystone reactive front, which evolves from the saw-tooth reactive front. The effects of activation energy on unstable ODW structure were examined systematically by Choi et al. [30]. The different structures of shock/combustion interaction under the different transition patterns was numerical investigated by Yang et al. [31] using reactive

Euler equations with a two-step hydrogen-air chemical reaction. Additionally, the effects of equivalence ratio on OSW-ODW transition structure in kerosene air mixture flows were investigated numerically by Ren et al. [32,33] based on the Navier-Stokes equations with a two-step reaction model and the influence of equivalence ratio and incoming Mach number on the initiation length and transition pressure has been analyzed in detail.

In the present study, a thorough investigation of the effects of activation energy on OSW-ODW transition structure is carried out based on the open source program Adaptive Mesh Refinement in Object-oriented C++ (AMROC) [26,28,34–36]. Quasi-one-dimensional primitive variables governing equations along the streamline of oblique detonation are used to study the flow characteristics of the non-detonation reaction zone with different initiation structures. Novel features concerning thermal expansion within the non-detonation reaction zone during different types of OSW-ODW transitions are discussed in detail. The reaction length on the oblique wedge surface is estimated based on assumptions of the CVC and CPC in the non-detonation zone, and the reaction length of the theoretical analysis is compared with numerical simulation results.

The paper is organized as follows. Section 2 summarizes the governing equations for the simulations and the numerical methods used to solve these equations. In Section 3, the numerical method is validated using a low-activation-energy case. Three types of oblique detonation transitions are studied numerically as a function of activation energy: smooth, weak, and strong-abrupt transition oblique detonations. Furthermore, with the assumption of CVC or CPC in the non-detonation zone, the reaction length on the oblique wedge surface is estimated and compared quantitatively with numerical simulation results. Section 4 contains our conclusions.

## 2. Numerical methods

### 2.1. Governing equations

The reactive Euler equations can be written as:

$$\begin{aligned} \frac{\partial \rho}{\partial t} + \frac{\partial}{\partial x_j} (\rho u_j) &= 0, \\ \frac{\partial (\rho u_i)}{\partial t} + \frac{\partial}{\partial x_j} (\rho u_i u_j + p \delta_{ij}) &= 0, \\ \frac{\partial (\rho E)}{\partial t} + \frac{\partial}{\partial x_j} [u_j (\rho E + p)] &= 0, \\ \frac{\partial (\rho Z)}{\partial t} + \frac{\partial}{\partial x_j} (\rho u_j Z) &= \rho \dot{\omega}, \end{aligned} \quad (1)$$

where  $\rho$  is the density,  $u_i$  is the component of velocity in the  $x_i$ -direction,  $p$  is the pressure,  $\delta_{ij}$  is the Kronecker symbol ( $\delta_{ij} = 1$  if  $i = j$ , and  $\delta_{ij} = 0$  otherwise), and  $Z$  is the mass fraction of product.  $E$  is the total energy is given by:

$$E = \frac{RT}{\gamma - 1} + \frac{1}{2} (u_i u_j) - Z Q, \quad (2)$$

where  $Q$  is the heat release,  $R$  is the universal gas constant,  $T$  is the temperature, and  $\gamma$  is the ratio of specific heats at a constant pressure and volume. The chemical reaction is modeled by a single-step irreversible reaction as follows:

$$\dot{\omega} = \kappa (1 - Z) \exp \left( -\frac{E_a}{RT} \right), \quad (3)$$

where  $\kappa$  is a pre-exponential factor (frequency factor) and  $E_a$  is the activation energy. The equation of state for an ideal gas mixture is:

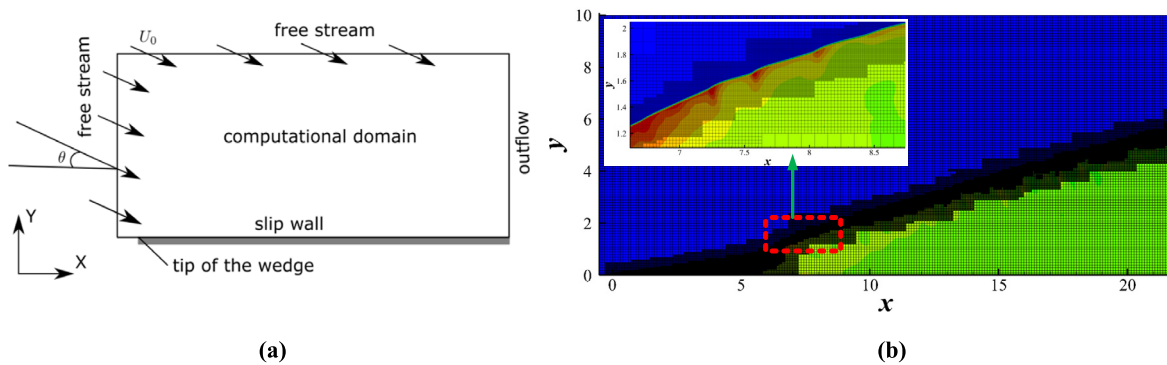


**Fig. 1.** Schematic of the computational domain, boundary conditions, and adaptive mesh structures. **(a)** Computational model; **(b)** Adaptive mesh structures.

$$p = \rho RT \quad (4)$$

Following reference of Deiterding [34], the thermodynamic and hydrodynamic quantities of reactant can be non-dimensionalized using the free stream values  $\rho_0$ ,  $p_0$ , and  $T_0$  for density, pressure, and temperature, so:

$$\tilde{\rho} = \frac{\rho}{\rho_0}, \quad \tilde{p} = \frac{p}{p_0}, \quad \tilde{T} = \frac{T}{T_0}, \quad (5)$$

resulting in the following normalizations for the thermodynamic and hydrodynamic quantities:

$$\tilde{E} = \frac{E}{RT_0}, \quad \tilde{E}_a = \frac{E_a}{RT_0}, \quad \tilde{Q} = \frac{Q}{RT_0}, \quad \tilde{u} = \frac{u}{\sqrt{RT_0}}. \quad (6)$$

The distances and times are further normalized in the problem as follows:

$$\tilde{x} = \frac{x}{L_{1/2}/\tilde{\kappa}}, \quad \tilde{t} = \frac{t\sqrt{RT_0}}{L_{1/2}/\tilde{\kappa}}, \quad \tilde{\kappa} = \frac{\kappa}{\sqrt{RT_0}}. \quad (7)$$

Hence, the non-dimensional transport equation for the product mass fraction becomes:

$$\frac{\partial(\tilde{\rho}Z)}{\partial\tilde{t}} + \frac{\partial}{\partial\tilde{x}_j}(\tilde{\rho}\tilde{u}_jZ) = L_{1/2}\tilde{\rho}(1-Z)\exp\left(-\frac{\tilde{E}_a}{\tilde{T}}\right), \quad (8)$$

where the non-dimensionalized value of the pre-exponential factor  $L_{1/2}$  is chosen so that the half-reaction length of a planar Chapman-Jouguet (CJ) detonation is unity. For notational simplicity, the tildes are omitted, and all variables are understood to be non-dimensionalized in the remainder of this paper.

The reactive Euler equation in two dimensions can be written concisely as follows:

$$\frac{\partial \mathbf{Q}}{\partial t} + \frac{\partial \mathbf{F}}{\partial x} + \frac{\partial \mathbf{G}}{\partial y} = \mathbf{S}, \quad (9)$$

where

$$\mathbf{Q} = \begin{pmatrix} \rho \\ \rho u \\ \rho v \\ \rho E \\ \rho Z \end{pmatrix}, \quad \mathbf{F} = \begin{pmatrix} \rho u \\ \rho u^2 + p \\ \rho uv \\ u(\rho E + p) \\ \rho u Z \end{pmatrix}, \quad \mathbf{G} = \begin{pmatrix} \rho v \\ \rho vu \\ \rho v^2 + p \\ v(\rho E + p) \\ \rho v Z \end{pmatrix},$$

$$\mathbf{S} = \begin{pmatrix} 0 \\ 0 \\ 0 \\ 0 \\ \rho \dot{\omega} \end{pmatrix}.$$

$\mathbf{Q}$  is a column vector of conservative flow variables, and  $\mathbf{F}$  and  $\mathbf{G}$  are the inviscid flux vectors in the  $x$ - and  $y$ -directions, respectively;  $\mathbf{S}$  is the reaction source term.

## 2.2. Numerical scheme

Numerical simulations were carried out using the open-source code AMROC [35,37] based on a structured adaptive mesh refinement (SAMR) framework [38]. An operator splitting technique (or, the method of fractional steps) for the computation of the time-dependent reactive flow [39] is used to solve Eq. (9). This technique allows a decoupled treatment for the time-implicit discretization of the source term and the time-explicit discretization of the hydrodynamic transport term. The convection terms in Eq. (9) are discretized using the seventh-order WENO-symmetric-order optimized (WENO-SYMOO) scheme, as shown by Martin et al. [40]. An optimal third-order strong stability preserving (SSP) Runge-Kutta scheme [41] is used for the time integration in combination with a time-splitting and fourth-order accurate semi-implicit GRK4A method [42] for source term integration.

## 2.3. Simulation settings and computational domain

Fig. 1 shows the two-dimensional computational domain and boundary conditions for the wedge-induced oblique detonation simulations. A horizontal wedge surface is employed, and Cartesian grids are aligned with the wedge surface. Free-stream conditions are imposed in both the left and upper boundaries of the domain as follows:

$$p_0 = 1, \quad \rho_0 = 1, \quad u_0 = 8 \cos \theta, \quad v_0 = -8 \sin \theta, \quad Z = 0, \quad (10)$$

where  $u_0$  and  $v_0$  are the components of the inflow velocity in the  $x$ - and  $y$ -directions, respectively. Slip-boundary conditions are employed at the wedge surface. Outflow conditions are imposed on the right boundary. The wedge angle is  $\theta = 25^\circ$ , and the chemistry parameters are set as  $\gamma = 1.3$ ,  $Q = 10$ , and  $E_A = 30$ .

## 3. Results and discussion

### 3.1. Numerical validation and grid independence study

For the low-activation-energy case,  $E_A = 20$  is used to keep the oblique detonation steady. The computational domain is  $(-0.5, 30)$  and  $(0, 15)$  in the  $x$ - and  $y$ -directions, respectively. The tip of the wedge is located at  $(0, 0)$ . An adaptive grid refinement algorithm is employed. The adaptive grid has  $(300 \times 150)$  cells at the coarsest level and four additional levels of refinement (5 levels grid mesh) with a ratio of 2. This provides a resolution of 40 points per half-reaction length (pts/hrl) of a CJ detonation.

To validate the numerical scheme, the numerical results are compared with those using the method of characteristics (MoC) [11,16]. The MoC is an exact method for steady supersonic flow when the number of characteristics is sufficient.

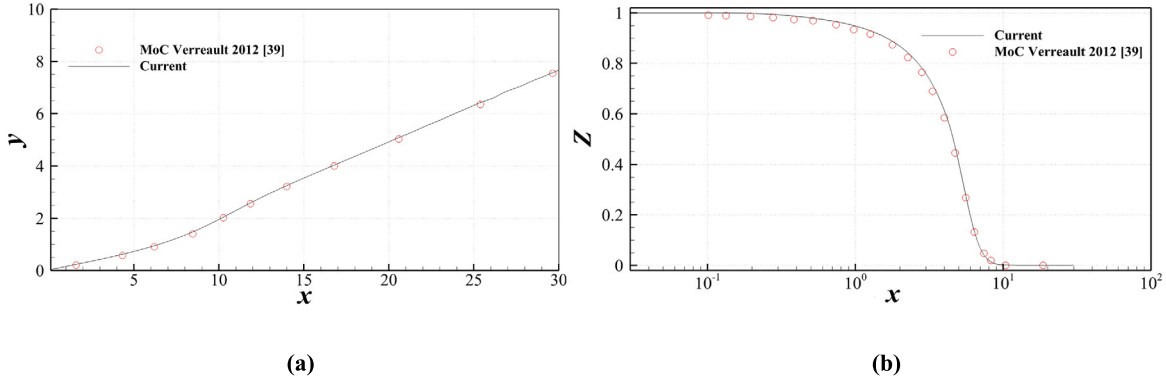


**Fig. 2.** Low-activation-energy case ( $E_A = 20$ ). (a) Shock trajectory; (b) Mass fraction of reactant along the wedge surface.

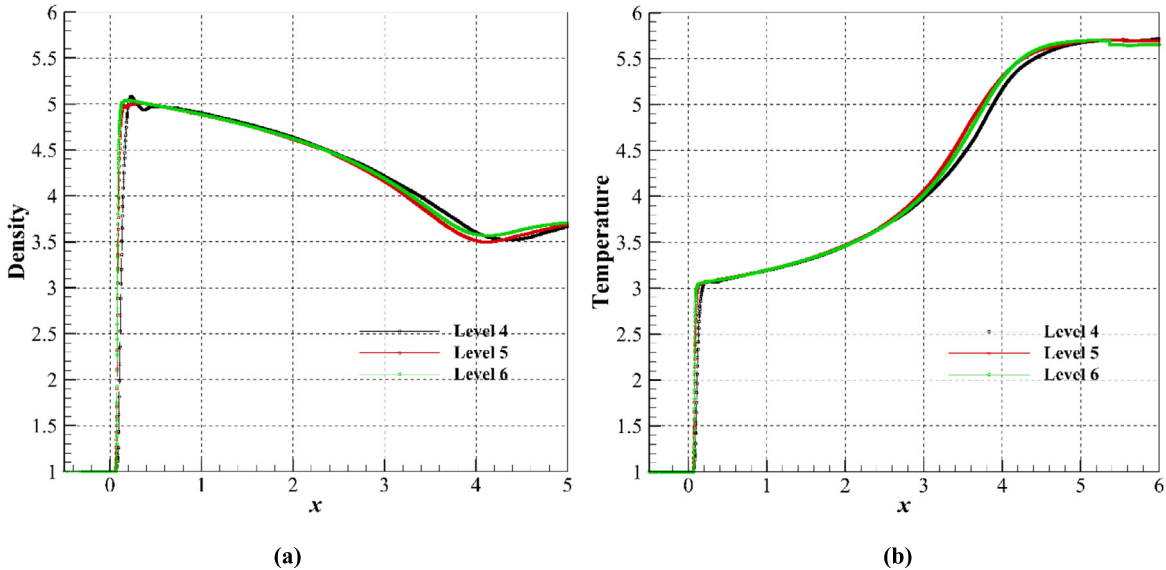


**Fig. 3.** Grid independence study for the higher activation energy case ( $E_A = 30$ ). (a) Density; (b) Temperature. (For interpretation of the colors in the figures, the reader is referred to the web version of this article.)

When a reactive supersonic inflow passes through a wedge, the induced oblique detonation angle  $\beta$  is given by the following equation [1]:

$$\frac{\tan(\beta - \theta)}{\tan \beta} = \frac{1 + \gamma M_{0n}^2 - \sqrt{(M_{0n}^2 - 1)^2 - 2(\gamma^2 - 1) M_{0n}^2 \frac{Q}{\gamma T_0}}}{(\gamma + 1) M_{0n}^2} \quad (11)$$

where  $M_{0n} = M_0 \sin \beta$ , and  $M_0$  is the inflow Mach number. Solving Eq. (11) using the given inflow and chemical parameters reveals that the theoretical oblique detonation angle is  $40.0^\circ$ .

Figs. 2(a) and 2(b) show the shock trajectory and the profile of the reaction progress variable along the wedge surface for the low-activation-energy case. The AMROC solutions are in excellent agreement with the MoC results [11].

To test mesh convergence, three different refinement levels of grid resolution (i.e. 4, 5, and 6 levels grid mesh) are considered for the higher activation energy case ( $E_A = 30$ ). Fig. 3 shows the density and temperature profiles along the wedge surface with the three grid systems. In the last two grid levels of 5 and 6, the temperature and density distributions are almost the same. Fig. 4 shows the temperature contours with 4, 5 and 6 levels grid in the range of  $-0.5 < x < 8$ . It is found that the temperature contours with 5 and 6 levels grid in the initiation zone are almost the same. To balance the calculation resolution and cost, the 5 levels grid is

selected for the current simulations with different activation energies.

### 3.2. Low-activation-energy case

ODWs can be classified into two transition types based on transition structure, i.e., smooth and abrupt transitions. The main difference between the two is that an abrupt-type transition can produce a triple point structure as the OSW transits to the ODW. However, for a smooth-transition structure, the OSW transits to the ODW smoothly with no triple point. For an abrupt-type transition, a slip line parallel to the wedge surface is generated starting from a triple point. The slip line divides the reaction zone into an upper detonation zone and a lower non-detonation zone. The lower non-detonation zone can further be divided into an induction zone and a deflagration zone [18,43]. Similarly, for a smooth transition, as shown in Fig. 5, the reaction zone is divided into a detonation and a non-detonation zone, which are separated from one another by the dotted line in Fig. 5. The line is parallel to the wedge surface and passes through the largest shock angle point on the leading shock wave.

For a simulation with a detailed chemical reaction model, the induction zone is defined as the area where the temperature maintains a nearly constant value behind the leading shock wave in the  $x$ -direction [18]. However, with a simplified single-step reac-

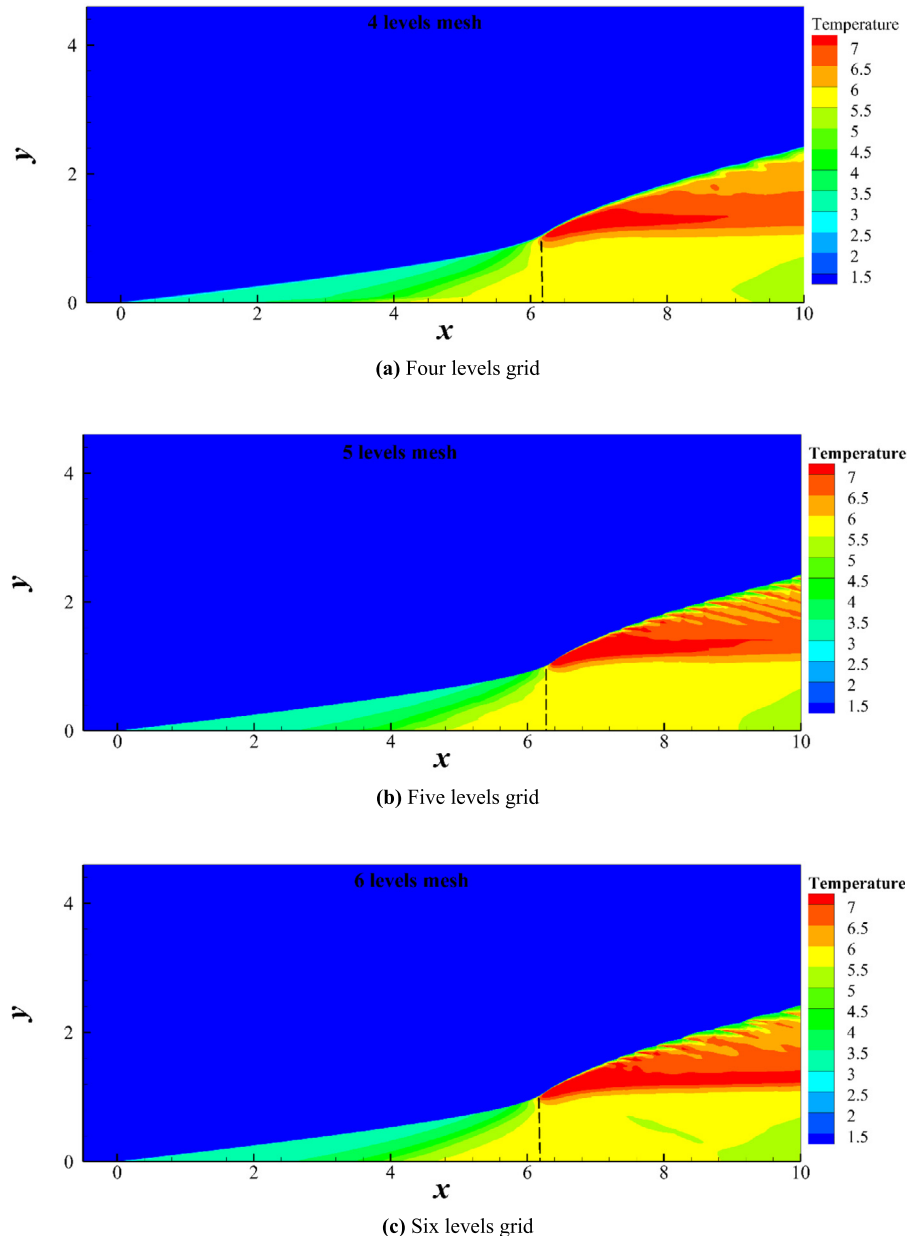


**Fig. 4.** Temperature contour with 4, 5 and 6 levels grid.

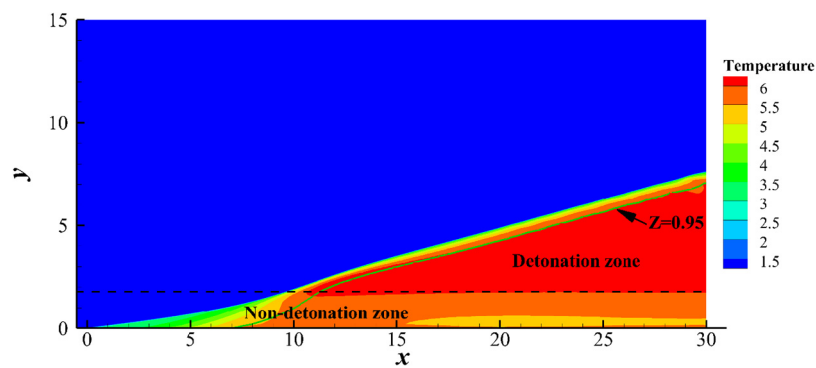


**Fig. 5.** Reaction zone for a smooth transition structure.

tion model, the induction zone is not well defined because the temperature continues to increase before the reaction has finished. Hence, instead of defining the induction length of detonation, the

reaction length in the non-detonation zone is defined in this paper as the distance between the leading shock wave to the  $Z=0.95$  contour in the  $x$ -direction.

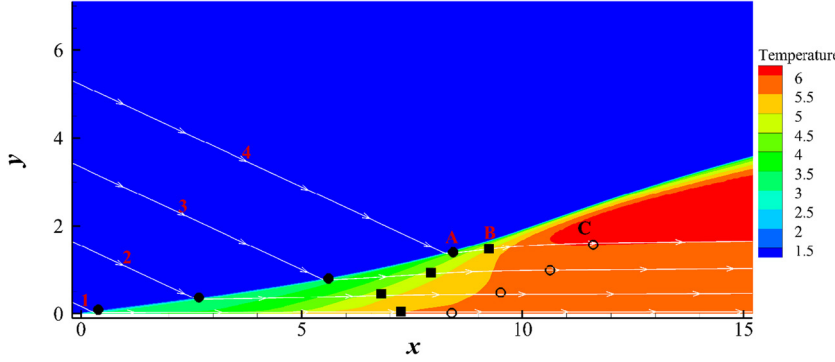


**Fig. 6.** Four streamlines in the non-detonation reaction zone in a smooth transition ( $E_A = 20$ ).

Usually, the reason for a reduction in induction length along the  $y$ -direction in an abrupt-type transition is because fluids are compressed in the induction zone as compression waves propagate upward along the local Mach angle [18,20].

To analyze the reduction in reaction length in the non-detonation zone, steady quasi-one-dimensional primitive variables governing equations (see Appendix A) are adopted. For a simplified single-step reaction model, the governing equations can be written as:

$$\frac{\partial Z}{\partial \xi} = \frac{1}{U} L_{1/2} (1 - Z) \exp\left(-\frac{E_a}{T}\right) \quad (12)$$

$$\frac{\partial \rho}{\partial \xi} = \frac{\rho}{U(M^2 - 1)} \left( \dot{\sigma} - M^2 U \frac{\partial \theta}{\partial \eta} \right) \quad (13)$$

$$\frac{\partial U}{\partial \xi} = -\frac{1}{(M^2 - 1)} \left( \dot{\sigma} - U \frac{\partial \theta}{\partial \eta} \right) \quad (14)$$

$$\frac{\partial p}{\partial \xi} = \frac{\rho U}{(M^2 - 1)} \left( \dot{\sigma} - U \frac{\partial \theta}{\partial \eta} \right) \quad (15)$$

$$\begin{aligned} \frac{\partial T}{\partial \xi} &= \frac{T}{U(M^2 - 1)} \left[ (\gamma M^2 - 1) \dot{\sigma} - UM^2(\gamma - 1) \frac{\partial \theta}{\partial \eta} \right] \\ &= \underbrace{\frac{T(\gamma M^2 - 1)}{U(M^2 - 1)} \dot{\sigma}}_A - \underbrace{\frac{TM^2(\gamma - 1)}{(M^2 - 1)} \frac{\partial \theta}{\partial \eta}}_B \end{aligned} \quad (16)$$

where  $\xi$  is the arc length along a streamline, the  $\eta$  direction is normal to the  $\xi$  direction,  $U$  is the velocity along a streamline,  $\theta$  is the angle between a streamline and the  $x$ -direction, and  $\dot{\sigma}$  is the thermicity defined as:

$$\dot{\sigma} = L_{1/2} \frac{(\gamma - 1) Q (1 - Z)}{\gamma T} \exp\left(-\frac{E_a}{T}\right) \quad (17)$$

Equation (16) shows that the temperature derivative along a streamline ( $\partial T / \partial \xi$ ) is determined by the terms  $A$  and  $B$ , representing the effects of the chemical reactions and the hydrodynamics. Furthermore,  $\partial \theta / \partial \eta$  in term  $B$  is a measure of streamline divergence. To solve Eqs. (12)–(16) to obtain the reaction length along a streamline  $\xi$ , the distribution of  $\partial \theta / \partial \eta$  needs to be determined. From Eq. (A.6) in Appendix A,  $\partial \theta / \partial \eta$  can be written as:

$$-U \frac{\partial \theta}{\partial \eta} = \frac{1}{\rho} \frac{\partial(\rho U)}{\partial \xi} \quad (18)$$

Substituting Eq. (18) into Eq. (16) results in:

$$\frac{\partial T}{\partial \xi} = \underbrace{\frac{T(\gamma M^2 - 1)}{U(M^2 - 1)} \dot{\sigma}}_A + \underbrace{\frac{TM^2(\gamma - 1)}{U(M^2 - 1)} \frac{1}{\rho} \frac{\partial(\rho U)}{\partial \xi}}_B \quad (19)$$

For the supersonic flow considered in this paper, Eq. (19) shows that, due to  $M > 1$ ,  $\gamma > 1$ , and  $\dot{\sigma} \geq 0$ , term  $A$  always has a positive value. Furthermore, if  $\partial(\rho U) / \partial \xi > 0$ , it means that the streamline converges, and that term  $B$  has a positive value. Otherwise,  $\partial(\rho U) / \partial \xi < 0$  means that the streamline diverges, and that term  $B$  has a negative value. A positive term  $A$  or term  $B$  makes the temperature increase along the streamline.

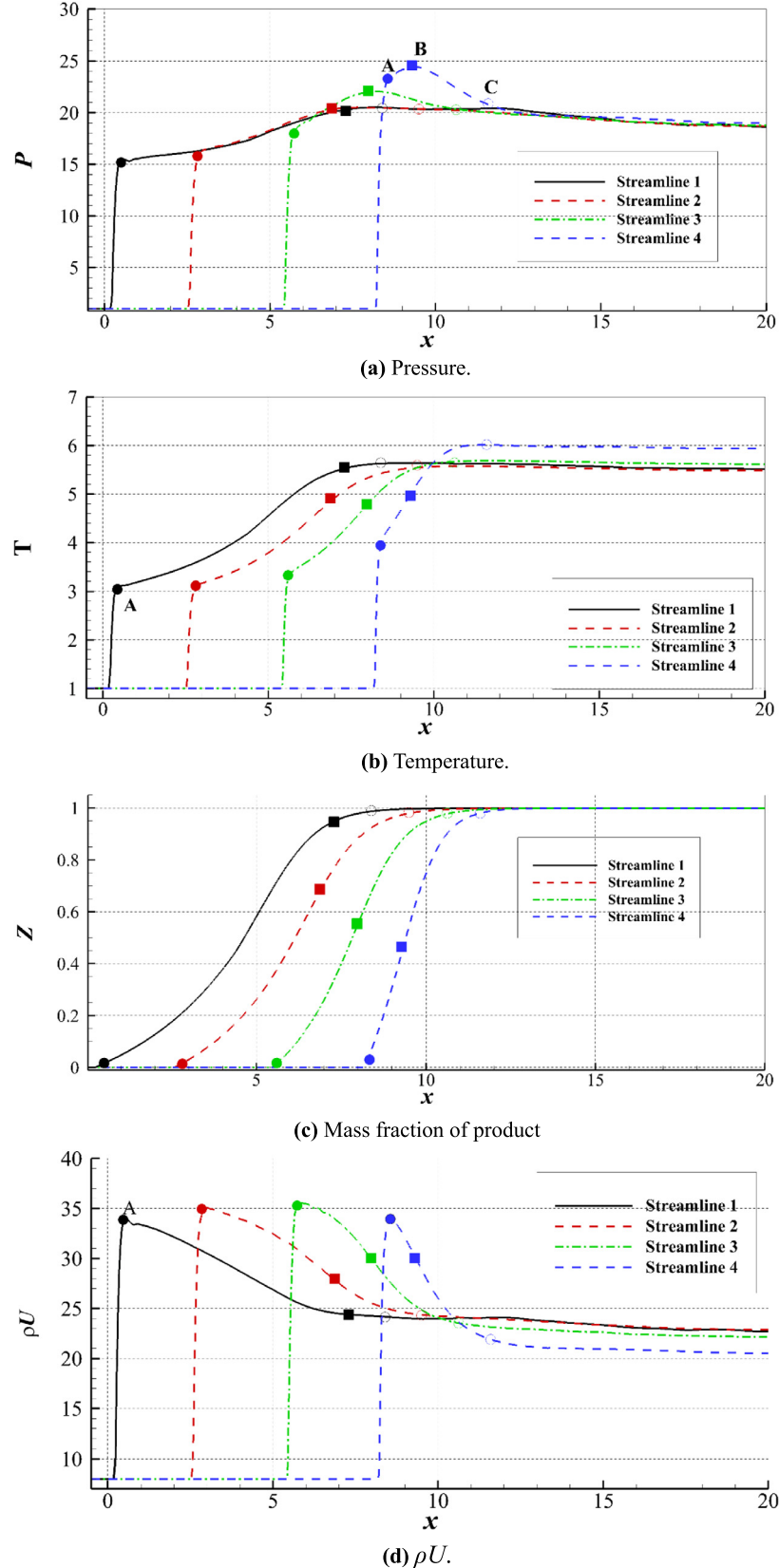
Fig. 6 shows four streamlines in the non-detonation reaction zone in a smooth transition. Fig. 7 shows the profiles of pressure, temperature, mass fraction of product, and  $\rho U$  along the four streamlines in Fig. 6. Point A, B and C in Figs. 6 and 7 are on the leading shock wave, the OSW-ODW transition region and the non-detonation reaction zones respectively, marked with a small solid circle ●; a small solid square ■ and a small hollow circle ○. (The three points A, B, and C in the following figure are all located at the same regions, and the marked symbols are the same.) Figs. 7(a) and 7(b) show that the pressure waves interact with the leading shock, steepen it, and contribute to the increase in pressure and temperature on point A along the  $y$ -direction, as the pressure waves propagate upward. Fig. 7(c) shows that the reaction length ( $0 < Z < 0.95$ ) decreases along the  $y$ -direction. It can be seen that the temperature, pressure and mass fraction increase from the leading shock wave (Point A) to the OSW-ODW transition region (Point B), but the velocity flux  $\rho U$  in the Fig. 7(d) is decreasing, and all parameters in the non-detonation reaction zone (Point C) are maintained within a certain range. Figs. 7(a) and 7(d) show that the fluids are in an expansion state along all four streamlines in the reaction zone ( $\partial(\rho U) / \partial \xi < 0$ ), although the pressure increases along the four streamlines.

Fig. 8 shows the profiles of term  $A$  and term  $B$  in Eq. (19) along the four streamlines in Fig. 6. It is not surprising that term  $A$  has positive values and term  $B$  has negative values along the four streamlines. The positive term  $A$  increases the temperature, and the negative term  $B$  decreases the temperature along the four streamlines. When terms  $A$  and  $B$  are equal, the temperature does not change, although a chemical reaction will still occur ( $Z < 1$ ). Fig. 8 also shows that the magnitude of term  $A$  is larger than that of term  $B$  before a balance has been reached, which means that the temperature has increased in this area.

From the above analyses, it can be concluded that the fluids in the reaction zone are in an expansion state instead of a compression state for a smooth transition. The increase in temperature on the steepened leading shock wave along the  $y$ -direction is the main cause of the reduction in reaction length in the non-detonation reaction zone.

### 3.3. Medium-activation-energy case

In this case, the activation energy has been increased to  $E_A = 30$  and five levels of refinement are used. This provides a resolution of 160 points per half-reaction length (pts/hrl) of a CJ



**Fig. 7.** Profiles of pressure, temperature, mass fraction of product, and  $\rho U$  along the four streamlines in Fig. 6.

detonation. The other computational parameters remain the same. Fig. 9 shows the temperature contour, leading shock wave, and  $Z = 0.95$  contour when the simulation is in a steady state. As in the low-activation-energy case, shown in Fig. 5, the OSW is

steepened due to the interactions between the pressure waves and the leading shock wave, as the pressure waves propagate upward. However, there are two differences flow characteristics in the non-detonation zones between these two cases: One is the appearance

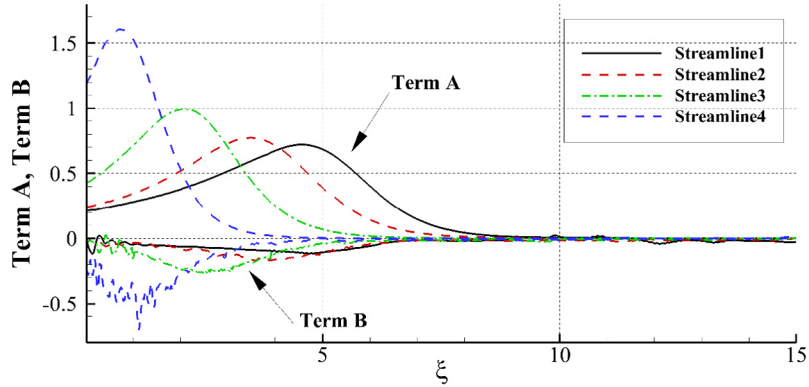


**Fig. 8.** Profiles of term *A* and term *B* in Eq. (19) along the four streamlines in Fig. 6.

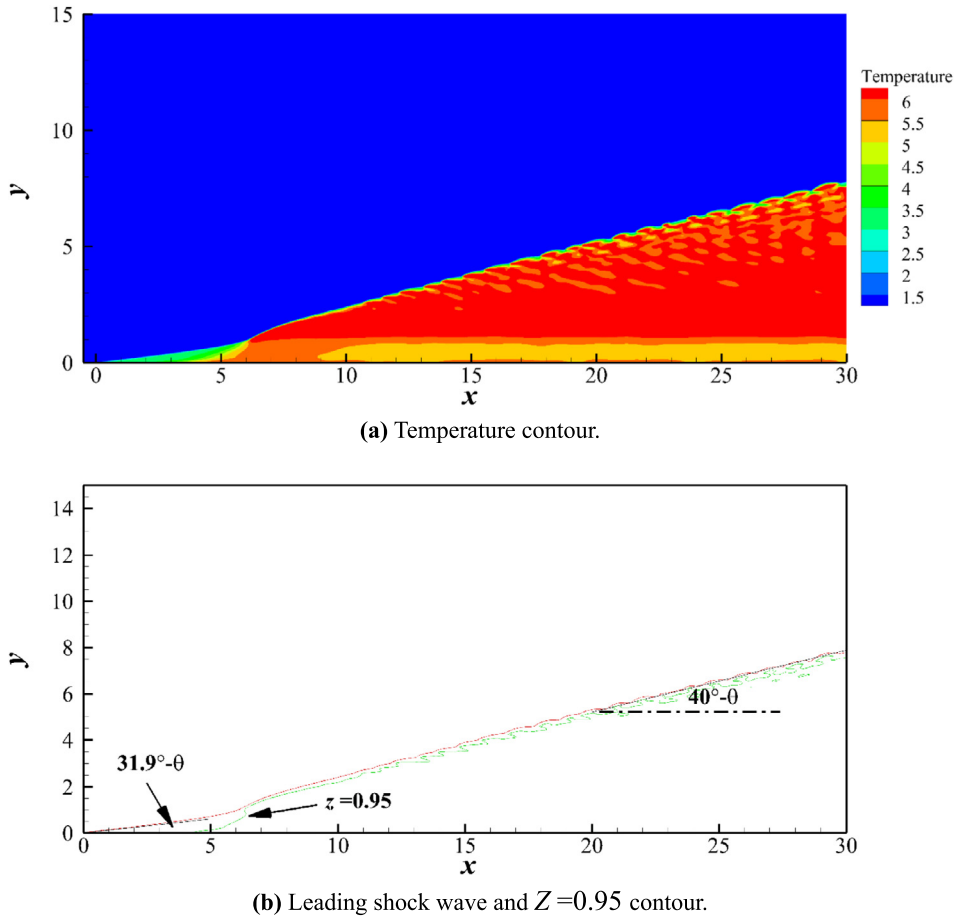


**Fig. 9.** Temperature contour, the leading shock wave, and the  $Z = 0.95$  contour for the medium-activation-energy case ( $E_A = 30$ ).

of an abrupt point on the leading shock wave for the higher activation energy case; the other is that the ODW oscillates up and down along the straight line with a theoretical angle of  $40^\circ$ .

Fig. 10 shows the four streamlines in the non-detonation reaction zone for the medium-activation-energy case. Fig. 11 shows the profiles of  $\rho U$ , pressure, temperature, and mass fraction of product along the four streamlines in Fig. 10. Compared with the low-activation-energy case, the fluids below streamline 2 in Fig. 11(a) are still in an expansion state ( $\partial(\rho U)/\partial\xi < 0$ ). However, above streamline 2, the fluids are gradually compressed as the pressure waves propagate upward. This increases the temperature on point B along the  $y$ -direction, which reduces the reaction length. As a result, OSW-ODW transition is completed faster. Moreover, both the deflagrative and transverse waves are weak, which is associated with a weak abrupt-type transition. It can be seen from the Figs. 11(b-d) that the changing trends of temperature, pressure and mass fraction about the points A, B and C are similar to the low-activation-energy case.

Fig. 12 shows the profiles of term *A* and term *B* in Eq. (19) along the four streamlines in Fig. 10. Along the  $y$ -direction, term *B*, ahead of the main reaction zone, makes more of a contribution to the increase in temperature. For the weak abrupt-type transition, there are two main reasons for the reduction in reaction length along the  $y$ -direction: One is that the steepened OSW increases the temperature at the points on the OSW as the pressure waves propagate upward; the other is that the propagating upward pressure waves compress fluids ahead of the main reaction zone, further increasing the temperature.

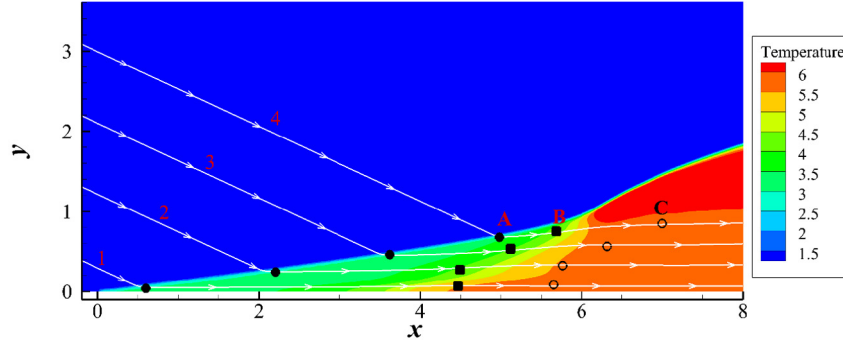


**Fig. 10.** Four streamlines in the non-detonation reaction zone for the medium-activation-energy case ( $E_A = 30$ ).

### 3.4. High-activation-energy case

In this case, the activation energy is further increased to  $E_A = 40$ . The grid at the coarsest level has  $(300 \times 150)$  cells and four additional levels of refinement to obtain finer grid resolutions. Furthermore, the computational domain is reduced to  $(-0.5, 10)$ ,  $(0, 5)$  in the  $x$ - and  $y$ -directions, respectively. This corresponds to a resolution of 240 points per half-reaction length (pts/hrl) of a CJ detonation.

Fig. 13 shows the temperature,  $Z = 0.95$  contour, and numerical schlieren of the density for this case. Compared with the temperature contour of the medium-activation-energy case in Fig. 9(a), the deflagration and transverse waves are stronger. This high-activation-energy case is a strong-abrupt transition.

Fig. 14 shows four streamlines in the non-detonation reaction zone for the high-activation-energy case. Fig. 15 shows the profiles of the  $\rho U$ , pressure, temperature, and mass fraction of product along the four streamlines in Fig. 14. Compared with the medium-activation-energy case in Fig. 10, there are generally similar distributions of these parameters along the streamlines. Fluids near the wedge surface are still in an expansion state in the reaction zone for this high-activation-energy case. As the pressure waves propagate upward, the fluids ahead of the main reaction zone (zones from point A to B) become more compressed. The compressed fluids make positive contributions to the increase in temperature along the streamlines, which reduces the reaction length along the  $y$ -direction. However, Figs. 15(b) and 15(c) show that Point A's pressure and temperature on the four streamlines remain almost constant. This means the pressure waves have fewer effects on the OSW in the high-activation-energy case. It can be seen from Fig. 7 (low-activation-energy case), Fig. 11 (medium-activation-energy case) and Fig. 15 (high-activation-energy case) that the pressure, temperature, and product mass fraction increase from point A to point B, and all parameters are maintained at a certain value at point C. As the activation energy increases, the temperature, pressure and  $\rho U$  on the points C all increase slightly.

Fig. 16 shows the profiles of term A and term B in Eq. (19) along the four streamlines in Fig. 14. Term B contributes more to the increase in temperature along the  $y$ -direction than that of the medium-activation-energy case. Some values of term B are even larger than those of term A on streamlines 3 and 4 due to the highly compressed fluids on these zones. In a strong-abrupt transition, the main reason for the reduction in reaction length along the  $y$ -direction is that fluids become more compressed ahead of the main reaction zone as pressure waves propagate upward.

### 3.5. Evaluation of the reaction length on the wedge surface

To evaluate the reaction length on the wedge surface, it is usually assumed that the reaction on the wedge surface is CVC ( $\partial\rho/\partial\xi = 0$ , density is supposed to keep constant), and the fluid

**Table 1**

Numerical and theoretical reaction lengths along the wedge surface.

$E_A$	Numerical	CVC	Error <sub>CVC</sub> (%)	CPC	Error <sub>CPC</sub> (%)
20	6.77	5.44	19.6	7.15	5.6
30	3.72	3.04	18.3	4.17	12.1
40	2.78	1.95	29.8	2.68	3.6

velocity is constant [21,44]. According to the quasi-one-dimensional primitive variables governing equations, Eqs. (12)–(16), the distribution of  $\rho U$  along the wedge surface must be determined to evaluate the reaction length. With the assumption of CVC ( $\partial\rho/\partial\xi = 0$ ) within the non-detonation zone, the density governing equation, Eq. (13), can be written as:

$$UM^2 \frac{\partial\theta}{\partial\eta} = \dot{\sigma} \quad (20)$$

Substituting Eq. (20) into temperature governing equation (16) gives:

$$\frac{\partial T}{\partial\xi} = \frac{T}{U} \gamma \dot{\sigma} \quad (21)$$

Assuming a constant fluid velocity ( $\partial U/\partial\xi = 0$ ) along the wedge surface, Eq. (21) and the mass fraction of product equation, Eq. (12), can be solved together to obtain the reaction length (from  $Z = 0$  to  $Z = 0.95$ ) along the wedge surface.

When assuming a constant fluid velocity without the consideration of CVC in the non-detonation zone, velocity governing equation (14) can be rewritten as:

$$U \frac{\partial\theta}{\partial\eta} = \dot{\sigma} \quad (22)$$

By substituting Eq. (22) into temperature governing equation (16) gives:

$$\frac{\partial T}{\partial\xi} = \frac{T}{U} \dot{\sigma} \quad (23)$$

Comparing the velocity equation, Eq. (14), with the pressure equation, Eq. (15), it shows that the assumption of constant velocity is equivalent to the assumption of constant pressure. Hence, Eq. (23) can also be considered as a temperature governing equation in CPC. Similarly, Eq. (23) and the mass fraction of product equation, Eq. (12), can be solved together to obtain the reaction length.

Table 1 shows the numerical and theoretical reaction lengths in CVC and CPC with different activation energies. The reaction lengths in CPC are in better agreement with the numerical results than those in CVC. Fig. 17 shows the density and velocity profiles along the wedge surface for the low-activation-energy case

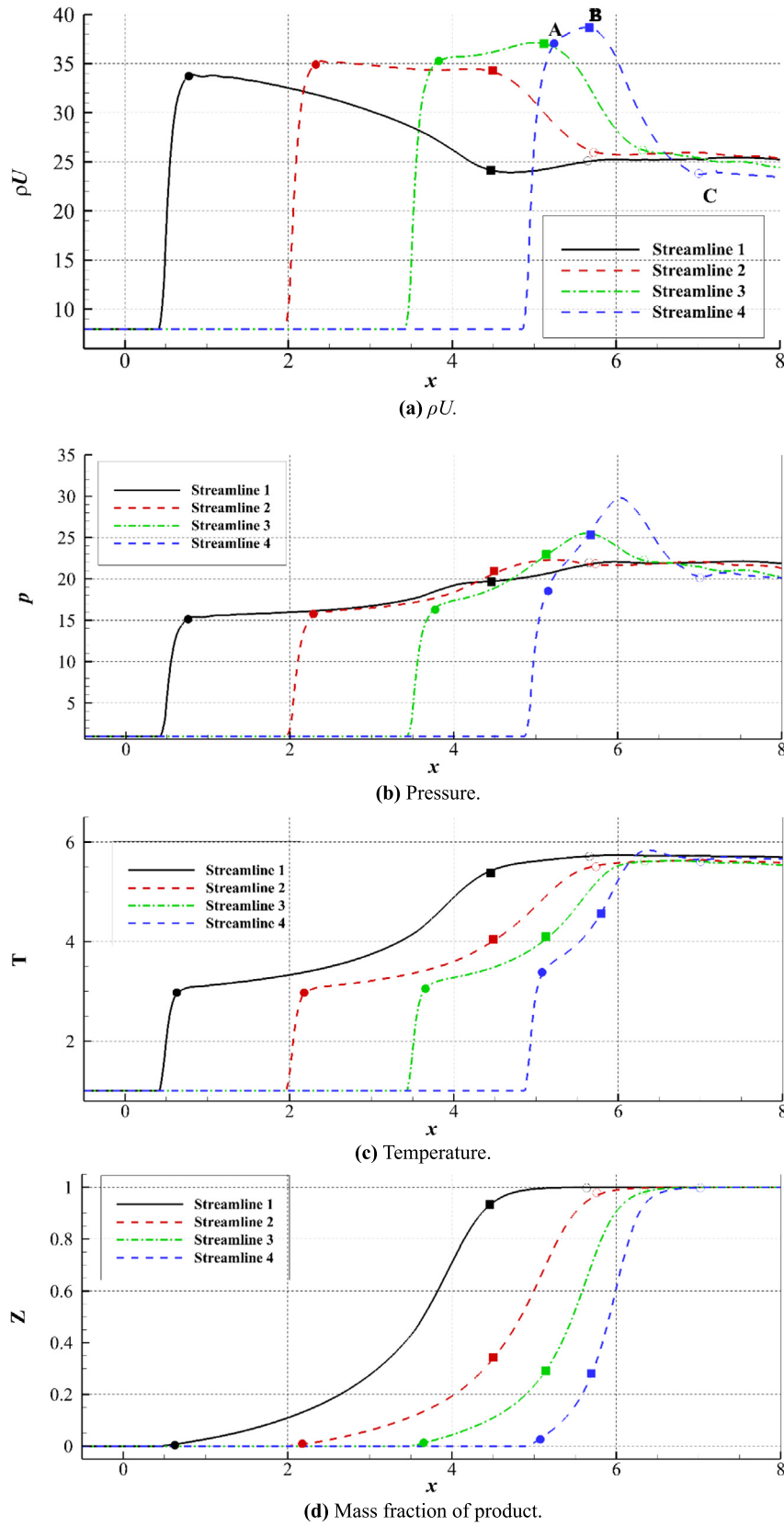


**Fig. 11.** Profiles of  $\rho U$ , pressure, temperature, and mass fraction of product along the four streamlines in Fig. 10.

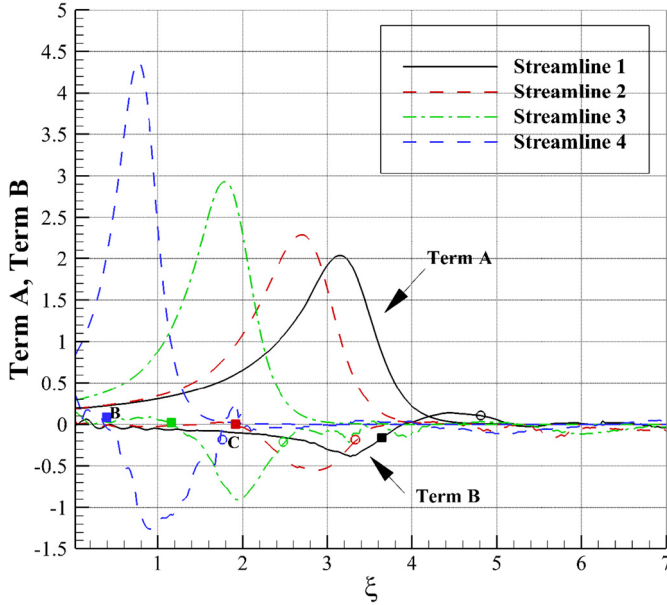


**Fig. 12.** Profiles of term *A* and term *B* in Eq. (19) along the four streamlines in Fig. 10.

( $E_A = 20$ ). The velocity profile is much smoother than the density profile in the reaction zone, meaning the assumption of CPC is more appropriate than the assumption of CVC.

#### 4. Conclusions

In this study, two-dimensional simulations are carried out to study the effects of activation energy on the reaction zone structure of oblique detonation.

Using different activation energies, three types of oblique detonations transition are studied numerically: smooth, weak, and strong-abrupt transition oblique detonations. For a smooth transition, the fluid along the streamline in the entire non-detonation zone is in an expansion state. As pressure waves propagate upward, the interaction between them and the oblique shock results in a gradual increase in oblique shock angle, which is the main reason for the reduction in reaction length along the  $y$ -direction. With increasing activation energy, the smooth transition is changed to a weak-abrupt transition. For weak-abrupt transition, the fluid near the wedge surface is in a state of expansion. However, as the pressure waves are strengthened upward, the fluid ahead of the main reaction area in the non-detonation zone is further compressed, which raises the temperature on the streamline and accelerates the combustion reaction. Along the  $y$ -direction, a gradual increase in oblique shock angle and a gradual increase in fluid compression ahead of the main reaction zone are the two main causes of the reduction in reaction length along a streamline. As the activation energy is increased, the weak-abrupt transition changes to a strong-abrupt transition. For strong-abrupt transition, the fluid near the wedge surface is still in a state of expansion. Compared to weak oblique detonation, the pressure wave is strengthened sharply during upward movement. Therefore, the fluid compression ahead of the main reaction in the non-detonation zone increases sharply. Along the  $y$ -direction, the sharp increase in the degree of compression ahead of the main reaction zone is the main reason for the reduction in reaction length.

Based on the assumption of CVC or CPC within the non-detonation zones, the reaction length on the oblique wedge surface is estimated respectively. Comparing the reaction length of the theoretical analysis with the simulation results, the hypothesis of CPC

is more appropriate than the hypothesis of CVC along the inclined wedge surface.

#### Declaration of competing interest

The authors declare that they have no known competing financial interests or personal relationships that could have appeared to influence the work reported in this paper.

#### Data availability

The data that support the findings of this study are available from the corresponding author upon reasonable request.

#### Acknowledgements

This research is sponsored by National Natural Science Foundation of China (Grant No. 51876182 and 11972331), Fundamental Research Funds for the Central Universities of China (Grant No. 20720180058).

#### Appendix A. Governing equations in a two-dimensional Bertrand-intrinsic coordinate system

The Bertrand-intrinsic coordinate system is also called the shock-attached coordinate system and is extensively used in detonation shock dynamics [45–48]. The coordinate system is a special orthogonal curvilinear coordinate system in which the coordinates are either parallel or normal to the shock surface. Fig. A.1 shows the relationship between the two-dimensional Cartesian ( $x, y$ ) and Bertrand-intrinsic ( $\xi, \eta$ ) coordinate systems, where  $\eta = 0$  is a shock surface,  $\vec{R}$  is the position vector of an arbitrary point  $p$ ,  $\vec{i}$  and  $\vec{j}$  are the unit vectors in the  $x$ - and  $y$ -directions in the Cartesian coordinate system,  $\vec{t}$  and  $\vec{n}$  are the tangent and normal unit vectors of point  $p$  on the curve  $\eta = \text{const}$ , and  $\theta$  is the angle between  $\vec{t}$  and  $\vec{i}$ .

Eqs. (A.1)–(A.5) comprise the continuity equation, the momentum equations in  $\xi$  and  $\eta$  directions, the energy equation, and the mass fraction  $Y_i$  equation in a two-dimensional Bertrand-intrinsic coordinate system.

$$\frac{1}{1 + \eta\kappa} \left( \frac{\partial(\rho u_\xi)}{\partial \xi} + \kappa \rho u_\eta \right) + \frac{\partial(\rho u_\eta)}{\partial \eta} + \rho u_\xi \frac{\partial \theta}{\partial \eta} = 0 \quad (\text{A.1})$$

$$u_\xi \left( \frac{\partial u_\xi}{\partial \xi} + \kappa u_\eta \right) + u_\eta (1 + \eta\kappa) \frac{\partial u_\xi}{\partial \eta} - u_\eta^2 (1 + \eta\kappa) \frac{\partial \theta}{\partial \eta} + \frac{1}{\rho} \frac{\partial p}{\partial \xi} = 0 \quad (\text{A.2})$$

$$-\kappa u_\xi^2 + u_\xi \frac{\partial u_\eta}{\partial \xi} + (1 + \eta\kappa) \left( u_\xi u_\eta \frac{\partial \theta}{\partial \eta} + u_\eta \frac{\partial u_\eta}{\partial \eta} + \frac{1}{\rho} \frac{\partial p}{\partial \eta} \right) = 0 \quad (\text{A.3})$$

$$\frac{u_\xi}{1 + \eta\kappa} \frac{\partial H}{\partial \xi} + u_\eta \frac{\partial H}{\partial \eta} = 0 \quad (\text{A.4})$$

$$\frac{u_\xi}{1 + \eta\kappa} \frac{\partial Y_i}{\partial \xi} + u_\eta \frac{\partial Y_i}{\partial \eta} = \frac{W_i \dot{\omega}_i}{\rho}, \quad i = 1, \dots, K-1 \quad (\text{A.5})$$

where  $u_\xi$  and  $u_\eta$  are the velocities in the  $\xi$  and  $\eta$  directions, respectively; the curvature  $\kappa = -\frac{\partial \theta}{\partial \xi}$  and  $H$  is the total enthalpy.

Assuming the  $\xi$ -axis is a streamline, the governing equations, Eqs. (A.1)–(A.5), on the streamline ( $u_\eta = 0, \eta = 0$ ) can be simplified as:

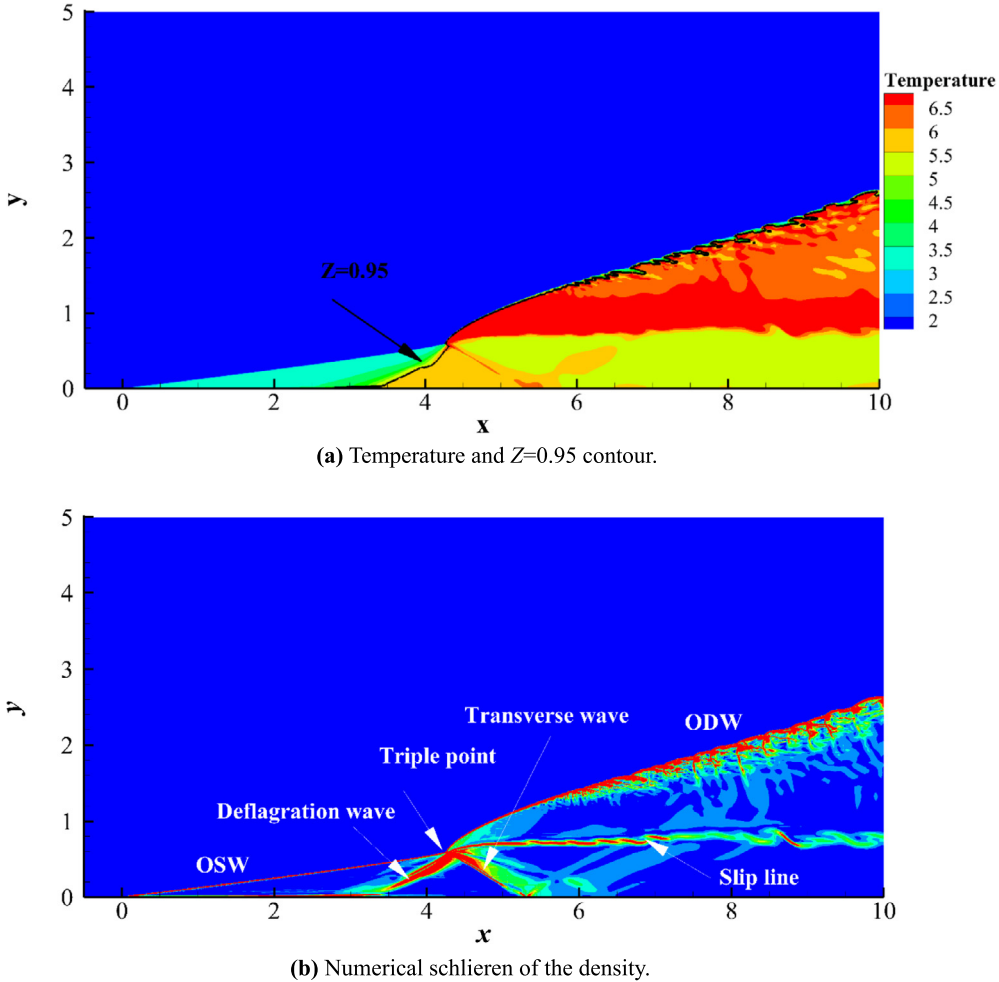


**Fig. 13.** Temperature,  $Z=0.95$  contour, and numerical schlieren of the density for the high-activation-energy case ( $E_A = 40$ ).

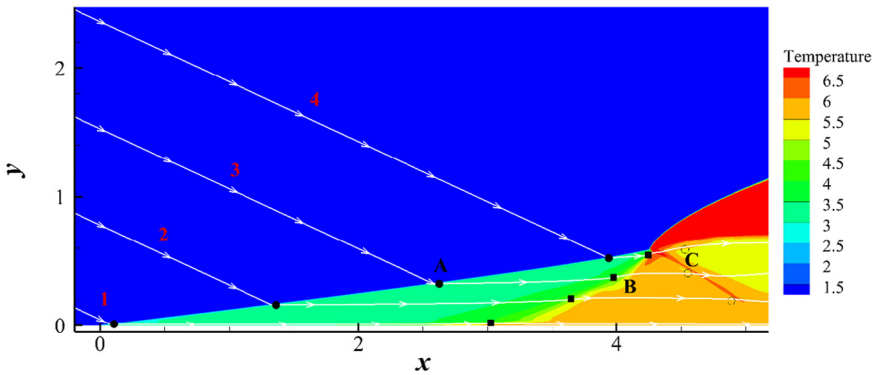


**Fig. 14.** Four streamlines in the non-detonation reaction zone for the high-activation-energy case ( $E_A = 40$ ).

$$\frac{\partial(\rho U)}{\partial \xi} + \rho U \frac{\partial \theta}{\partial \eta} = 0 \quad (\text{A.6})$$

$$\rho U \frac{\partial U}{\partial \xi} + \frac{\partial p}{\partial \xi} = 0 \quad (\text{A.7})$$

$$\rho U^2 \frac{\partial \theta}{\partial \xi} + \frac{\partial p}{\partial \eta} = 0 \quad (\text{A.8})$$

$$\frac{\partial H}{\partial \xi} = 0 \quad (\text{A.9})$$

$$U \frac{\partial Y_i}{\partial \xi} = \frac{W_i \dot{\omega}_i}{\rho} \quad (\text{A.10})$$

where  $U$  is the velocity along streamline  $\xi$ .

Following the derivative of the primitive variable governing equations in the Cartesian coordinate system [34], the conservative variable governing equations, Eqs. (A.6)–(A.10), along streamline  $\xi$  can be derived to the quasi-one-dimensional primitive variables governing equations:

$$\frac{\partial \rho}{\partial \xi} = \frac{\rho}{U(M^2 - 1)} \left( \dot{\sigma} - M^2 U \frac{\partial \theta}{\partial \eta} \right) \quad (\text{A.11})$$

$$\frac{\partial U}{\partial \xi} = -\frac{1}{(M^2 - 1)} \left( \dot{\sigma} - U \frac{\partial \theta}{\partial \eta} \right) \quad (\text{A.12})$$

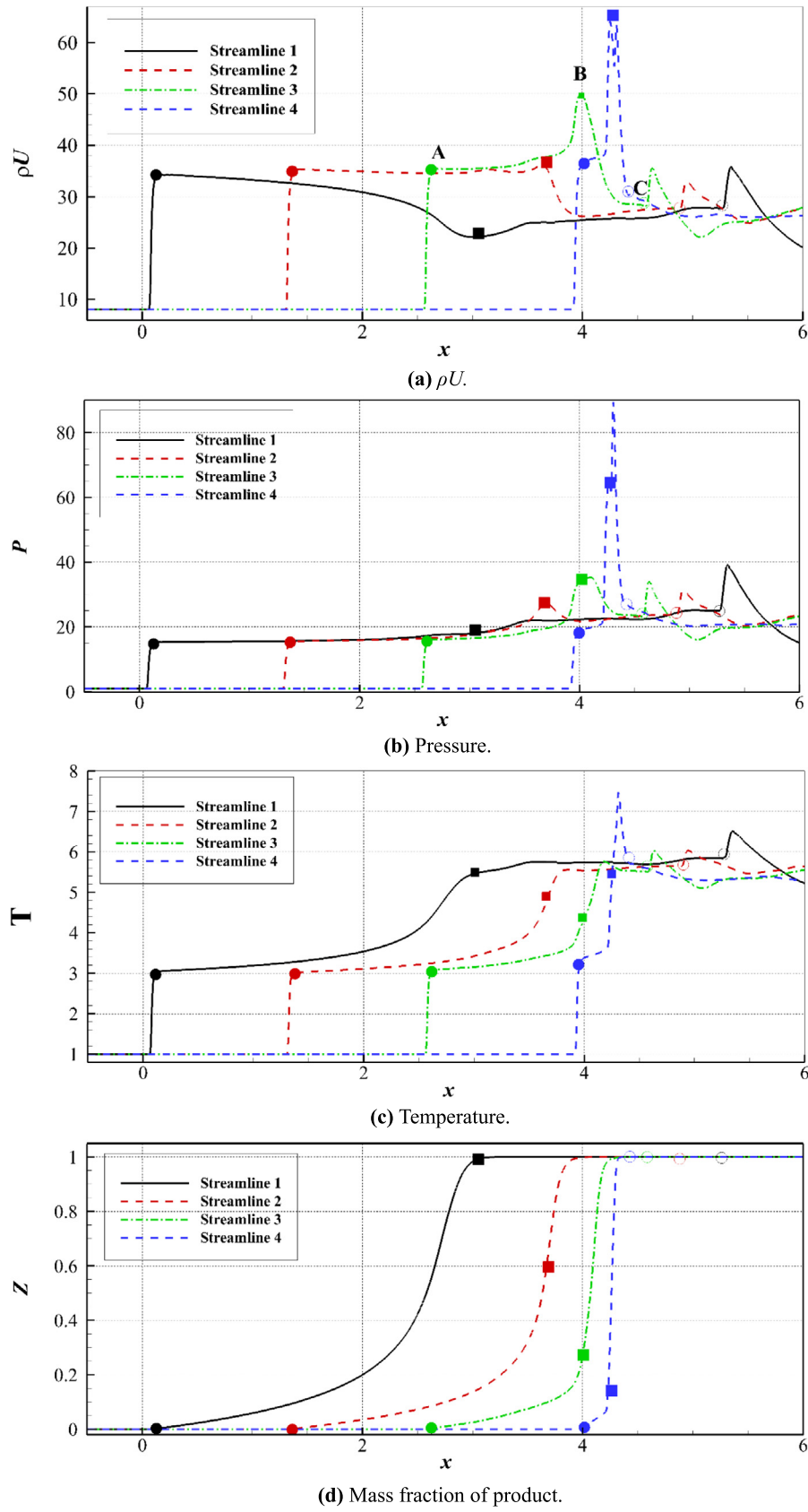


**Fig. 15.** Profiles of  $\rho U$ , pressure, temperature, and mass fraction of product along the four streamlines in Fig. 14.

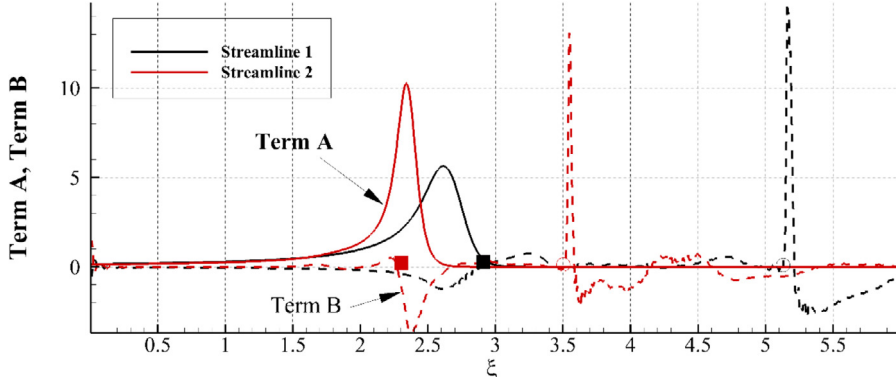
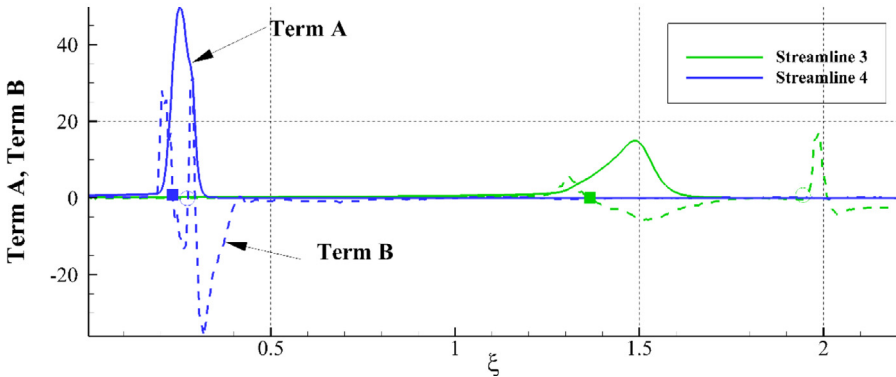
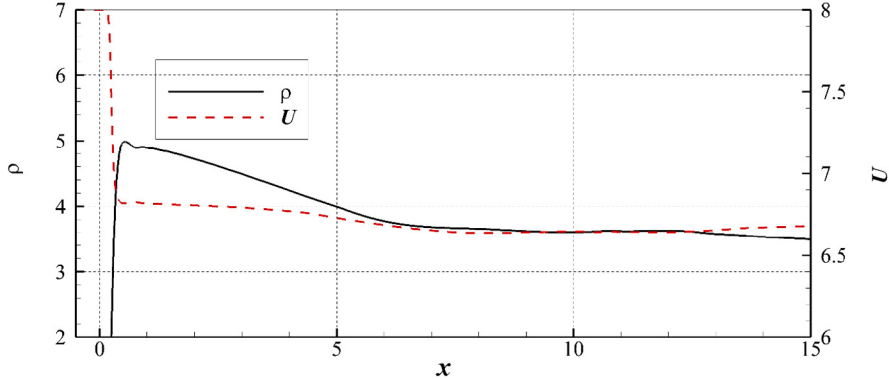
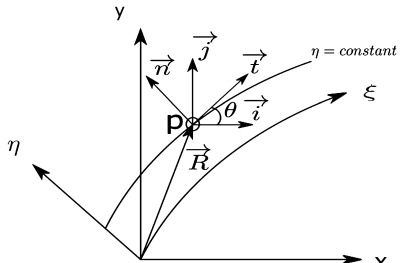
(a) Term *A* and term *B* along streamlines 1 and 2.(b) Term *A* and term *B* along streamlines 3 and 4.Fig. 16. Profiles of term *A* and term *B* in Eq. (19) along the four streamlines in Fig. 14.Fig. 17. Density and velocity profiles along the wedge surface for the low-activation-energy case ( $E_A = 20$ ).

Fig. A.1. Two-dimensional Bertrand-intrinsic coordinate system.

$$\frac{\partial p}{\partial \xi} = \frac{\rho U}{(M^2 - 1)} \left( \dot{\sigma} - U \frac{\partial \theta}{\partial \eta} \right) \quad (\text{A.13})$$

$$\frac{\partial T}{\partial \xi} = -\frac{T}{U(M^2 - 1)} \left[ \left( 1 - \gamma M^2 \right) \dot{\sigma} - UM^2 (1 - \gamma) \frac{\partial \theta}{\partial \eta} \right] \quad (\text{A.14})$$

$$+ \frac{W(M^2 - 1)}{\rho} \sum_{i=1}^K \dot{\omega}_i \Bigg] \quad (\text{A.14})$$

where  $\dot{\sigma}$  is the thermicity:

$$\dot{\sigma} = \sum_{i=1}^K \sigma_i \frac{W_i \dot{\omega}_i}{\rho}, \quad \sigma_i = \frac{W}{W_i} - \frac{h_i}{c_p T} \quad (\text{A.15})$$

For a simplified single-step irreversible reaction model, after non-dimensionalization using Eqs. (5)–(7), the quasi-one-dimensional primitive variables governing equations can be written as:

$$\frac{\partial Z}{\partial \xi} = \frac{1}{U} L_{1/2} (1 - Z) \exp \left( -\frac{E_a}{T} \right) \quad (\text{A.16})$$

$$\frac{\partial \rho}{\partial \xi} = \frac{\rho}{U(M^2 - 1)} \left( \dot{\sigma} - M^2 U \frac{\partial \theta}{\partial \eta} \right) \quad (\text{A.17})$$

$$\frac{\partial U}{\partial \xi} = -\frac{1}{(M^2 - 1)} \left( \dot{\sigma} - U \frac{\partial \theta}{\partial \eta} \right) \quad (\text{A.18})$$

$$\frac{\partial p}{\partial \xi} = \frac{\rho U}{(M^2 - 1)} \left( \dot{\sigma} - U \frac{\partial \theta}{\partial \eta} \right) \quad (\text{A.19})$$

$$\frac{\partial T}{\partial \xi} = \frac{T}{U(M^2 - 1)} \left[ \left( \gamma M^2 - 1 \right) \dot{\sigma} - U M^2 (\gamma - 1) \frac{\partial \theta}{\partial \eta} \right] \quad (\text{A.20})$$

## References

- [1] D.T. Pratt, J.W. Humphrey, D.E. Glenn, Morphology of standing oblique detonation waves, *J. Propuls. Power* 7 (5) (1991) 837–845.
- [2] J.M. Powers, K.A. Gonthier, Reaction zone structure for strong, weak overdriven, and weak underdriven oblique detonations, *Phys. Fluids* 4 (9) (1992) 2082–2089.
- [3] J.M. Powers, Oblique detonations: theory and propulsion applications, in: J. Buckmaster, T.L. Jackson, A. Kumar (Eds.), *Combustion in High-Speed Flows*, Kluwer Academic, Norwell, MA, 1994, pp. 345–371.
- [4] C.I. Morris, M.R. Kamel, R.K. Hanson, Shock-induced combustion in high-speed wedge flows, *Symp. (Int.) Combust.* 27 (2) (1998) 2157–2164.
- [5] D.S. Stewart, A.R. Kasimov, State of detonation stability theory and its application to propulsion, *J. Propuls. Power* 22 (6) (2006) 1230–1244.
- [6] J. Urzay, Supersonic combustion in air-breathing propulsion systems for hypersonic flight, *Annu. Rev. Fluid Mech.* 50 (2018) 593–627.
- [7] Y. Liu, L. Wang, B. Xiao, Z. Yan, C. Wang, Hysteresis phenomenon of the oblique detonation wave, *Combust. Flame* 192 (2018) 170–179.
- [8] R. Gross, Oblique detonation waves, *AIAA J.* 1 (5) (1963) 1225–1227.
- [9] J.M. Powers, D.S. Stewart, Approximate solutions for oblique detonations in the hypersonic limit, *AIAA J.* 30 (3) (1992) 726–736.
- [10] G. Emanuel, D.G. Tuckness, Steady, oblique, detonation waves, *Shock Waves* 13 (6) (2004) 445–451.
- [11] J. Verreault, A.J. Higgins, R.A. Stowe, Formation and structure of steady oblique and conical detonation waves, *AIAA J.* 50 (8) (2012) 1766–1772.
- [12] D. Martínez-Ruiz, C. Huete, A.L. Sánchez, F.A. Williams, Theory of weakly exothermic oblique detonations, *AIAA J.* 58 (1) (2020) 236–242.
- [13] D. Martínez-Ruiz, L. Scotzniovsky, A.L. Sanchez, F.A. Williams, Wedge-induced oblique detonations with small heat release, in: *AIAA Scitech 2021 Forum*, AIAA 2021-0287, <https://doi.org/10.2514/6.2021-0287>.
- [14] C. Viguier, L.F.F. da Silva, D. Desbordes, B. Deshaies, Onset of oblique detonation waves: comparison between experimental and numerical results for hydrogen-air mixtures, *Symp. (Int.) Combust.* 26 (1996) 3023–3031.
- [15] C. Viguier, A. Gourara, D. Desbordes, Three-dimensional structure of stabilization of oblique detonation wave in hypersonic flow, *Symp. (Int.) Combust.* 27 (1998) 2207–2214.
- [16] J. Verreault, Initiation of gaseous detonation by conical projectiles, Ph.D. thesis, McGill University, 2012.
- [17] Z. Jiang, Z. Zhang, Y. Liu, C. Wang, C. Luo, Criteria for hypersonic airbreathing propulsion and its experimental verification, *Chin. J. Aeronaut.* 34 (3) (2021) 94–104.
- [18] C. Li, K. Kailasanath, E.S. Oran, Detonation structures behind oblique shocks, *Phys. Fluids* 6 (4) (1994) 1600–1611.
- [19] V.V. Vlasenko, V.A. Sabel'nikov, Numerical simulation of inviscid flows with hydrogen combustion behind shock waves and in detonation waves, *Combust. Explos. Shock Waves* 31 (3) (1995) 376–389.
- [20] L.F.F. Da Silva, B. Deshaies, Stabilization of an oblique detonation wave by a wedge: a parametric numerical study, *Combust. Flame* 121 (1–2) (2000) 152–166.
- [21] H. Teng, H.D. Ng, Z. Jiang, Initiation characteristics of wedge-induced oblique detonation waves in a stoichiometric hydrogen-air mixture, *Proc. Combust. Inst.* 36 (2) (2017) 2735–2742.
- [22] Y. Fang, Z. Hu, H. Teng, Z. Jiang, H.D. Ng, Numerical study of inflow equivalence ratio inhomogeneity on oblique detonation formation in hydrogen-air mixtures, *Aerosp. Sci. Technol.* 71 (2017) 256–263.
- [23] P. Yang, H. Teng, Z. Jiang, H.D. Ng, Effects of inflow Mach number on oblique detonation initiation with a two-step induction-reaction kinetic model, *Combust. Flame* 193 (2018) 246–256.
- [24] M.V. Papalexandris, A numerical study of wedge-induced detonations, *Combust. Flame* 120 (4) (2000) 526–538.
- [25] H. Teng, Z. Jiang, On the transition pattern of the oblique detonation structure, *J. Fluid Mech.* 713 (2012) 659–669.
- [26] S. Miao, J. Zhou, S. Liu, X. Cai, Formation mechanisms and characteristics of transition patterns in oblique detonations, *Acta Astronaut.* 142 (2018) 121–129.
- [27] Y. Zhang, P. Yang, H. Teng, H.D. Ng, C. Wen, Transition between different initiation structures of wedge-induced oblique detonations, *AIAA J.* 56 (10) (2018) 4016–4023.
- [28] S. Miao, J. Zhou, Z. Lin, X. Cai, S. Liu, Numerical study on thermodynamic efficiency and stability of oblique detonation waves, *AIAA J.* 56 (8) (2018) 3112–3122.
- [29] Y. Zhang, L. Zhou, J. Gong, H.D. Ng, H. Teng, Effects of activation energy on the instability of oblique detonation surfaces with a one-step chemistry model, *Phys. Fluids* 30 (2018) 106110.
- [30] J.Y. Choi, D.W. Kim, I.S. Jeung, F. Ma, V. Yang, Cell-like structure of unstable oblique detonation wave from high-resolution numerical simulation, *Proc. Combust. Inst.* 31 (2) (2007) 2473–2480.
- [31] L. Yang, L. Yue, Q. Zhang, X. Zhang, Numerical study on the shock/combustion interaction of oblique detonation waves, *Aerosp. Sci. Technol.* 104 (2020) 105938.
- [32] Z. Ren, B. Wang, L. Zheng, Wedge-induced oblique detonation waves in supersonic kerosene-air premixing flows with oscillating pressure, *Aerosp. Sci. Technol.* 110 (2021) 106472.
- [33] Z. Ren, B. Wang, Numerical study on stabilization of wedge-induced oblique detonation waves in premixing kerosene-air mixtures, *Aerosp. Sci. Technol.* 107 (2020) 106245.
- [34] R. Deiterding, Parallel adaptive simulation of multi-dimensional detonation structures, Ph.D. thesis, Brandenburgische Technische Universität Cottbus, 2003.
- [35] R. Deiterding, A parallel adaptive method for simulating shock-induced combustion with detailed chemical kinetics in complex domains, *Comput. Struct.* 87 (11–12) (2009) 769–783.
- [36] H. Peng, Y. Huang, R. Deiterding, Z. Luan, F. Xing, Y. You, Effects of jet in crossflow on flame acceleration and deflagration to detonation transition in methane-oxygen mixture, *Combust. Flame* 198 (2018) 69–80.
- [37] J.L. Ziegler, R. Deiterding, J.E. Shepherd, D. Pullin, An adaptive high order hybrid scheme for compressive, viscous flows with detailed chemistry, *J. Comput. Phys.* 230 (20) (2011) 7598–7630.
- [38] M.J. Berger, J. Oliger, Adaptive mesh refinement for hyperbolic partial differential equations, *J. Comput. Phys.* 53 (3) (1984) 484–512.
- [39] E.S. Oran, J.P. Boris, *Numerical Simulation of Reactive Flow*, 2nd edition, Cambridge University Press, 2001.
- [40] M. Martín, E. Taylor, M. Wu, V. Weirs, A bandwidth-optimized WENO scheme for the effective direct numerical simulation of compressible turbulence, *J. Comput. Phys.* 220 (1) (2006) 270–289.
- [41] S. Gottlieb, D.I. Ketcheson, C.W. Shu, High order strong stability preserving time discretizations, *J. Sci. Comput.* 38 (3) (2008) 251–289.
- [42] P. Kaps, P. Rentrop, Generalized Runge-Kutta methods of order four with step-size control for stiff ordinary differential equations, *Numer. Math.* 33 (1) (1979) 55–68.
- [43] K. Ghorbanian, J.D. Sterling, Influence of formation processes on oblique detonation wave stabilization, *J. Propuls. Power* 12 (3) (1996) 509–517.
- [44] T. Wang, Y. Zhang, H. Teng, Z. Jiang, H.D. Ng, Numerical study of oblique detonation wave initiation in a stoichiometric hydrogen-air mixture, *Phys. Fluids* 27 (9) (2015) 096101.
- [45] H.G. Hornung, Gradients at a curved shock in reacting flow, *Shock Waves* 8 (1) (1998) 11–21.
- [46] D.S. Stewart, Lectures on detonation physics: introduction to the theory of detonation shock dynamics, *TAM Rep.* 721, UILU-ENG-93-6019, 1993.
- [47] J. Yao, S. Stewardt, On the normal detonation shock velocity curvature relationship for materials with large activation energy, *Combust. Flame* 100 (5) (1995) 19–528.
- [48] J. Yao, *The dynamics of multi-dimensional detonation*, Ph.D. thesis, Theoretical and Applied Mechanics, University of Illinois, 1996.